Nanoscale

PAPER

Check for updates

Optimizing active sites *via* chemical bonding of 2D metal–organic frameworks and MXenes for efficient hydrogen evolution reaction activity†

Anand P. Tiwari, [iD] ‡[a] Priyanshu Chandra, [iD] ‡[b] Md Saifur Rahman,[a] Katherine A. Mirica [iD] [b] and William J. Scheideler [iD] *[a]

Metal–organic frameworks (MOFs) are promising electrocatalysts due to their large surface areas and abundant metal sites, but their efficacy is limited by poor exposure of active metal atoms to the electrolyte. To address this issue, we report an innovative approach that integrates a conductive layered MXene ($Ti_3C_2T_x$) with a 2-dimensional (2D) Ni_3(2,3,6,7,10,11-hexaiminotriphenylene)$_2$-MOF through *in situ* synthesis of the MOF on the MXene, maximizing the accessible exposure of active sites for electrocatalytic hydrogen evolution reaction (HER) activity. XPS analysis confirms that the MOF is chemically bonded with the MXene layers, while SEM analysis shows complete overlapping, intercalation, and surface growth of the MOF on the MXene layers. The optimized chemically bonded MOF on MXene exhibits superior electrocatalytic activity, with an overpotential of 180 mV in alkaline media—four times better than that of the pristine MOF—and an overpotential of 240 mV in acidic media, three times better than that of the pristine MOF. The enhanced electrocatalytic activity is attributed to the bond formation between Ti atoms from the MXene and N atoms from the MOF, which facilitates charge transfer and improves both the kinetics and active electrocatalytic area for the HER. This method offers a simple, pioneering approach to fabricate noble metal-free, nanostructured electrocatalysts, enhancing water electrolysis efficiency and extending applicability to other conductive MOFs.

Introduction

Water electrolysis is a sustainable and promising alternative to traditional hydrogen production methods.[1] It boasts high catalytic efficiency, produces hydrogen of exceptional purity, and generates less pollution compared to conventional generation of H_2 from fossil fuels.[2] This process involves two main reactions: the hydrogen evolution reaction (HER) and the oxygen evolution reaction (OER). The HER progresses slowly, necessitating an efficient electrocatalyst to enhance the reaction rate.[3] Although Pt/C is a top-performing electrocatalyst with excellent catalytic activity for the HER, its scarcity and high cost limit its widespread use.[4] Therefore, there is an urgent need to develop high-activity, low-cost electrocatalysts for the HER. In response to this challenge, researchers have conducted extensive studies

exploring transition metal derivatives such as transition metal phosphides,[5] metal nitrides,[6] alloys,[7] and metal oxides.[8] These materials have been investigated for their ability to effectively adsorb hydrogen, thereby enhancing reaction kinetics. Transition metal-based metal–organic frameworks (MOFs) are an emerging class of porous crystalline materials composed of metal ions or clusters coordinated with organic ligands. With their large porosity, diverse structures, and tunable compositions, MOFs have garnered significant attention in electrocatalysis.[9,10] Notably, MOFs incorporating Ni and Fe have demonstrated promising performances as electrocatalysts for the alkaline HER.[11] This is due to partial charge transfer between the transition metals and organic ligands in an alkaline medium, resulting in low overpotentials and stability comparable to state-of-the-art materials.[12–14] This interest arises from their facile synthesis, large specific surface areas, uniformly distributed metal nodes, and unique honeycomb-like π-conjugated structures. MOFs typically retain their porous architecture with a high density of active metal centers, thereby enhancing the electrocatalytic performance of the HER.[15] Two-dimensional (2D) MOFs, composed of transition metal (TM) atoms coordinated with organic ligands, represent a unique class of porous coordination polymers. Their large

*[a]Thayer School of Engineering, Dartmouth College, Hanover, NH 03755, USA.
E-mail: william.j.scheideler@dartmouth.edu
[b]Department of Chemistry, Burke Laboratory, Dartmouth College, Hanover, New Hampshire 03755, USA*
†Electronic supplementary information (ESI) available. See DOI: https://doi.org/10.1039/d5nr00550g
‡These authors contributed equally to this work.

surface area, excellent electrical conductivity, and tunable compositions have positioned them as promising candidates in the field of electrocatalysis.[16,17] Although bulk 2-dimensional (2D) MOFs exhibit electrical conductivity, a significant portion of their metal nodes are deeply embedded within the material, making them inaccessible to electrolytes.[18,19] Consequently, this limitation often results in their unsatisfactory performance during HER activity. To address these challenges, supporting a conductive MOF on a well-designed layered conductive matrix could be a potential solution. This approach would enhance accessibility to active sites and improve overall electrocatalytic performance for the HER.

Given their remarkable electronic conductivity, efficient charge transport, and cost-effectiveness, 2-dimensional (2D) MXene materials, particularly ($Ti_3C_2T_x$), are widely employed as charge transport materials to support active components and enhance electrochemical properties.[20,21] MXenes feature catalytically active basal planes with exposed metal sites, which can be functionalized with termination groups (T_x = O, OH, and F).[22,23] These groups provide sites for chemical bonding with other active materials, further enhancing their catalytic capabilities in various electrochemical applications.[24] Furthermore, 2D layered nanostructures of MXenes exhibit large surface areas and diverse elemental combinations.[25] These characteristics not only facilitate efficient electron and mass transfer across solid–liquid–gas interfaces, but also provide significant flexibility in designing hybrid materials. Thus, combining an MXene and an MOF *via* chemical bonding can be an effective strategy to develop highly active electrocatalysts. In this context, the terminal groups from the MXene can facilitate chemical bonding between the anionic ligand functionality from the MOF and cationic metal sites from the MXene.[26] This interaction can create an effective charge transfer pathway, enhancing the kinetics of electrocatalytic activity. The metal in the MXene can bond with anion atoms, synergistically optimizing the adsorption energies of intermediates at active sites, thereby achieving efficient HER performance.[24,26,27] For example, N-doping can enhance the electrocatalytic activity of Ti-based MXenes for the HER by up to two times.[23,24] Additionally, this molecular design strategy has the potential to address the issue of metal atom inaccessibility to electrolytes, thereby improving the efficiency of HER activity. Given these considerations, the combination of conductive MOFs—particularly single-metallic 2D Ni-based MOFs—with MXenes represents a promising strategy for advancing the development of nanostructures with enhanced HER activity in both acidic and alkaline media. This improvement arises from the increased number of accessible metal sites within the MOF and the strong interaction between MOF anion atoms and the MXene, which facilitates charge transfer and optimizes active site exposure for efficient electrocatalysis.

Herein, we report a facile *in situ* strategy for preparing an $Ni_3(2,3,6,7,10,11-hexaiminotriphenylene)_2$-MOF ($Ni_3(HITP)_2$-MOF) and $Ti_3C_2T_x$-MXene layered heterostructure. This approach creates a hybrid material with multiple HER active sites and enhances the pathway for charge transfer, resulting

in excellent HER performance in both alkaline and acidic electrolytes. The nitrogen (N) atoms from the MOF ligands chemically bond with the titanium (Ti) in the MXene, completely enveloping the MXene layers, intercalating between them, and growing on their surfaces. Electrostatic interactions between the nitrogen atoms (anions) and titanium ions have been reported,[28] through which the terminating atoms (O, OH, F) of $Ti_3C_2T_x$-MXene act as active sites, coordinating the nitrogen atoms with titanium ions. This chemical bonding facilitates charge transfer and maximizes the active area, improving kinetics and electrochemical coverage for the HER. The chemically bonded MOF on the MXene in this study shows high electrocatalytic activity, with an overpotential of 180 mV at 10 mA cm^{-2} and a Tafel slope of 123 mV dec^{-1} in alkaline media, as well as a low overpotential of 240 mV at 10 mA cm^{-2} in acidic media. Additionally, it exhibits excellent durability, sustaining the HER for over 150 hours. This method presents a straightforward yet innovative approach for producing noble metalfree, layered nanostructured electrocatalysts. It effectively enhances water electrolysis efficiency and broadens the applicability to other conductive MOFs.

Results and discussion

The synthesis route of chemically bonded $Ni_3(HITP)_2@Ti_3C_2T_x$ is illustrated in Fig. 1(a). The $Ti_3C_2T_x$-MXene layers were synthesized by following a recently reported method (see the Experimental section in the ESI† for details).[24] Then, a Nibased metal–organic framework ($Ni_3(HITP)_2$) is coated and intercalated onto the MXene layers using 2,3,6,7,10,11-hexaaminotriphenylene (HATP) and nickel(II) acetate ($Ni(OAc)_2$) *via* a simple solvothermal method[29] (synthesis of the MOF is shown in ESI Fig. S1†). Finally, the $Ni_3(HITP)_2$ on MXene is converted into chemically bonded $Ni_3(HITP)_2@Ti_3C_2T_x$ *via* annealing under forming gas (95% N_2 + 5% H_2) at 200 °C. The ratio between $Ni_3(HITP)_2$-MOF and $Ti_3C_2T_x$-MXene was varied by adjusting the amounts of HATP and $Ti_3C_2T_x$ starting materials to achieve fully coated and intercalated $Ni_3(HITP)_2$ within the $Ti_3C_2T_x$ layers. We synthesized four different layered heterostructures with different ratios of HATP and $Ti_3C_2T_x$: 2 : 1, 1 : 1, 2 : 3, and 1 : 4, denoted as MOF@$Ti_3C_2T_x$(66%HATP), MOF@$Ti_3C_2T_x$(50%HATP), MOF@$Ti_3C_2T_x$(33%HATP), and MOF@$Ti_3C_2T_x$(25%HATP), respectively. The heat-treated sample is denoted as MOF@$Ti_3C_2T_x$(Ti–N).

Scanning electron microscopy (SEM) and transmission electron microscopy (TEM) were carried out to analyze the morphology and structure of $Ni_3(HITP)_2@Ti_3C_2T_x$. The as-synthesized $Ti_3C_2T_x$-MXene shows a well-stacked layered structure, as shown in Fig. 1(b) (the SEM images of pristine MOF are shown in ESI Fig. S2†). In contrast, the optimized $Ni_3(HITP)_2@Ti_3C_2T_x$ (MOF@$Ti_3C_2T_x$(33%HATP)) exhibits a grass-like morphology on a large scale, consisting of continuous thin-layered structures with abundant wrinkles of $Ni_3(HITP)_2$-MOF, grown on the top surface and intercalated between the layers of $Ti_3C_2T_x$-MXene, as shown in Fig. 1(c) and
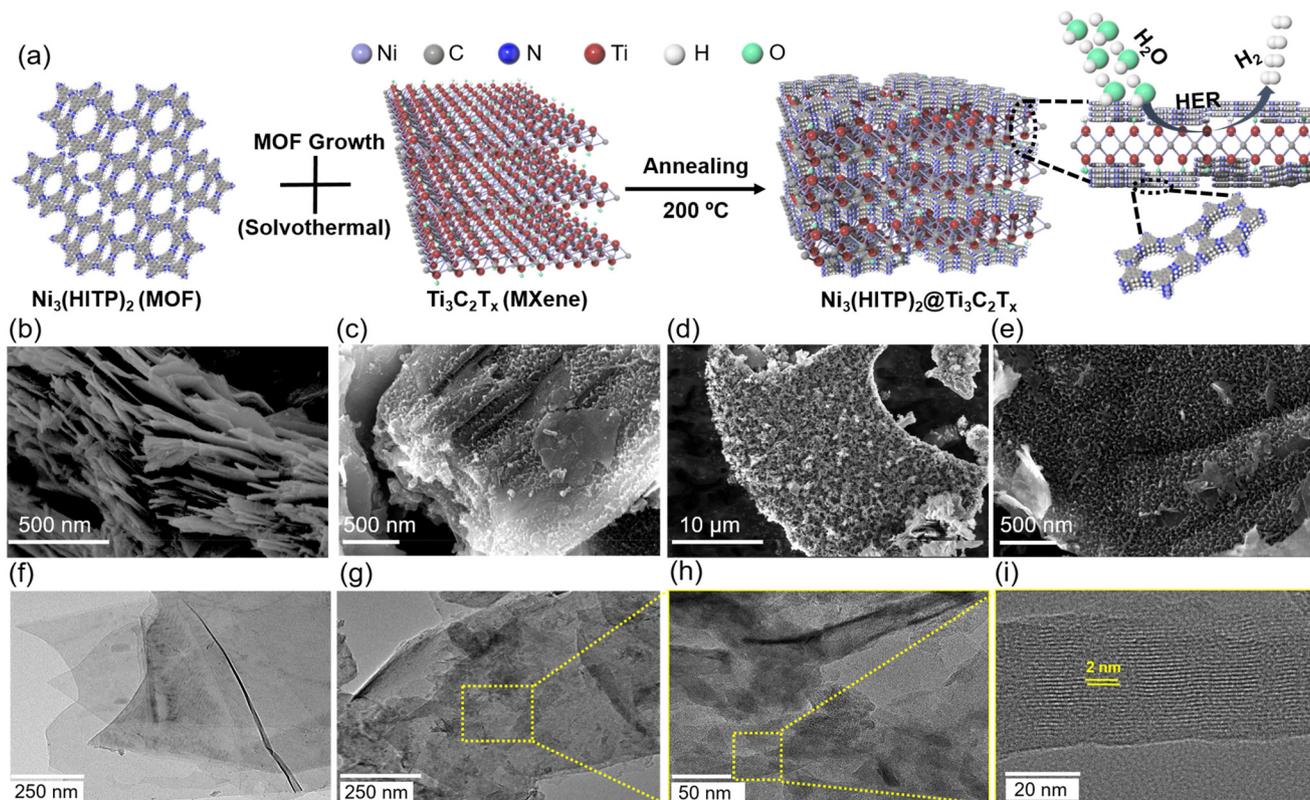
Fig. 1 (a) Schematic illustration of the fabrication process of chemically bonded $Ni_3(HITP)_2@Ti_3C_2T_x$. The inset shows HER activity on chemically bonded $Ni_3(HITP)_2@Ti_3C_2T_x$. SEM images of (b) pristine $Ti_3C_2T_x$-MXene, and (c–e) $Ni_3(HITP)_2@Ti_3C_2T_x$. TEM images of (f) pristine $Ti_3C_2T_x$-MXene, and (g–i) $Ni_3(HITP)_2@Ti_3C_2T_x$.

(d). The interaction of $Ni_3(HITP)_2$-MOF with $Ti_3C_2T_x$-MXene creates an extensively hierarchical porous structure, with pore sizes in the range of tens of nanometers. The grass-like structure of $Ni_3(HITP)_2@Ti_3C_2T_x$ is composed of stacked nanoparticles with widths of about 10–20 nm and lengths of 100–200 nm. This unique porous morphology efficiently increases electroactivity by exposing active centers and allowing rapid mass diffusion between $Ni_3(HITP)_2$-MOF and $Ti_3C_2T_x$-MXene nanosheets. Unlike the optimized MOF@$Ti_3C_2T_x$(33%HATP), with its $Ni_3(HITP)_2@Ti_3C_2T_x$ structure, the heterostructures with other ratios of MOF and MXene (MOF@$Ti_3C_2T_x$(66%HATP), MOF@$Ti_3C_2T_x$(50%HATP), and MOF@$Ti_3C_2T_x$(25%HATP)) did not show continuous coverage of MOF on MXene (as shown in ESI Fig. S3†). Similar to the SEM analysis, the TEM images reveal that optimized $Ni_3(HITP)_2@Ti_3C_2T_x$ consists of smooth, velvet-like layered structures (Fig. 1(f–i)). The as-synthesized $Ti_3C_2T_x$-MXene shows semitransparent layered structures, as shown in Fig. 1(f). However, the optimized $Ni_3(HITP)_2@Ti_3C_2T_x$ (MOF@$Ti_3C_2T_x$(33%HATP)) consists of continuous and well-dispersed 2D $Ni_3(HITP)_2$-MOF on $Ti_3C_2T_x$-MXene sheets, as shown in Fig. 1(g). Furthermore, the high-resolution transmission electron microscopy (HRTEM) images of $Ni_3(HITP)_2@Ti_3C_2T_x$ (Fig. 1(h, and i)) reveal clear lattice fringes with an interplanar spacing of 2.0 nm, corresponding

to the (100) plane of $Ni_3(HITP)_2$. A detailed examination shows distinct hexagonal lattice points representing Ni atoms (ESI Fig. S4†), with a ~2.0 nm spacing between adjacent pore centers. This observation is consistent with the crystal structure and agrees with reported theoretical atomic models.[30]

The X-ray diffraction (XRD) patterns of $Ni_3(HITP)_2@Ti_3C_2T_x$ are consistent with those of $Ni_3(HITP)_2$-MOF and $Ti_3C_2T_x$-MXene, as simulated from their crystal structures, confirming the successful growth of $Ni_3(HITP)_2$ on the MXene surfaces,[30,31] as shown in Fig. 2(a). The prominent peaks of $Ni_3(HITP)_2$ at 4.77° (100), 9.56° (200), and 27.48° (011) show its crystalline structure.[32] Meanwhile, each composition of $Ni_3(HITP)_2@Ti_3C_2T_x$ exhibits a prominent (002) peak of $Ti_3C_2T_x$-MXene at 8.80°, confirming the presence of 2D $Ti_3C_2T_x$-MXene, in line with the SEM and TEM results. It is noted that the (002) peak of $Ti_3C_2T_x$-MXene in all $Ni_3(HITP)_2@Ti_3C_2T_x$ compositions is slightly shifted towards a lower angle compared to that of pristine $Ti_3C_2T_x$-MXene (9.09°), indicating the intercalation of MOF between the layers of $Ti_3C_2T_x$-MXene. Moreover, the variation in peak intensities across different compositions of $Ni_3(HITP)_2$-MOF and $Ti_3C_2T_x$-MXene is attributed to the differing ratios of these components, while all major peaks are present in every composition.

It is interesting to observe that after heat treatment of the optimized MOF@$Ti_3C_2T_x$ composition (MOF@$Ti_3C_2T_x$(33%
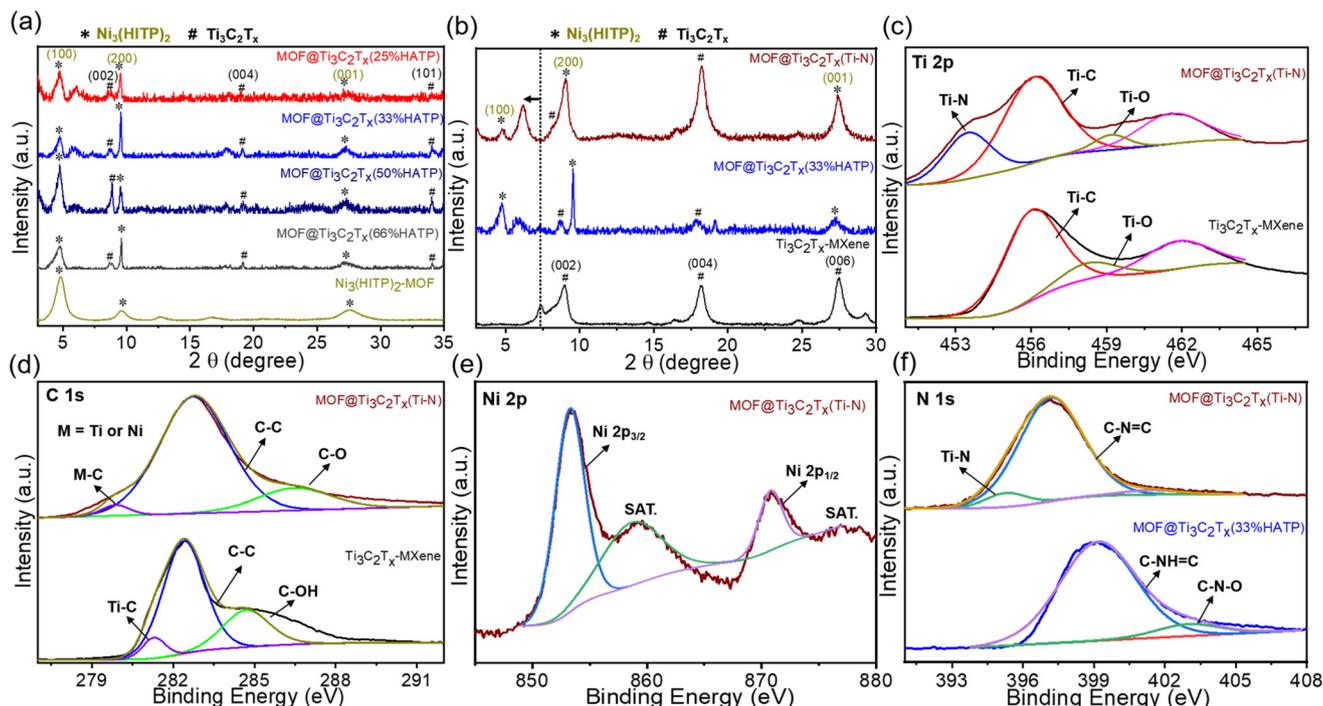
Fig. 2 Phase and chemical characterization of chemically bonded $Ni_3(HITP)_2@Ti_3C_2T_x$. (a) XRD patterns of $MOF@Ti_3C_2T_x$ synthesized using varying compositions of MXene and HATP, illustrating the structural evolution with different ratios. (b) XRD patterns of annealed $MOF@Ti_3C_2T_x$ (33% HATP) compared with pristine MXene, highlighting the peak shift in the MXene peak, which confirms the intercalation of MOF into MXene layers. High-resolution XPS spectra and fitting curves. (c) Ti 2p for $MOF@Ti_3C_2T_x$ (Ti–N) and pristine MXene, demonstrating the appearance of a new peak at lower binding energy in $MOF@Ti_3C_2T_x$ (Ti–N), which confirms the formation of Ti–N bonds. (d) C 1s for $MOF@Ti_3C_2T_x$ (Ti–N) and pristine MXene. (e) Ni 2p for $MOF@Ti_3C_2T_x$ (Ti–N). (f) N 1s for $MOF@Ti_3C_2T_x$ (33% HATP) before (bottom) and after annealing (top), demonstrating a shift toward lower binding energy in the annealed sample, which confirms the formation of Ti–N bonding.

HATP)), the peak at 7.41°, which corresponds to the intercalation of the terminating groups (O, OH, and F) in the MXene, shifts further towards a lower angle, as shown in Fig. 2(b). This peak shift further validates the substitution of the terminating groups in $Ti_3C_2T_x$ with intercalated $Ni_3(HITP)_2$-MOF between the MXene layers.[33] The valence state and chemical composition of $Ni_3(HITP)_2@Ti_3C_2T_x$ are analyzed using X-ray photoelectron spectroscopy (XPS) to further confirm the chemical bonding between MXene and $Ni_3(HITP)_2$-MOF. Compared to pristine $Ti_3C_2T_x$-MXene, a new characteristic peak at 453.5 eV, corresponding to Ti^{2+}, can be found in the Ti 2p XPS spectra of $MOF@Ti_3C_2T_x$(Ti–N) (Fig. 2(c)), suggesting the formation of Ti–N bonds.[34] With regard to the C 1s XPS spectra, the characteristic peaks of C–C/C=C bonds on the benzene ring at 284.5 eV indicate that the MOF structure is retained in $MOF@Ti_3C_2T_x$(Ti–N), as shown in Fig. 2(d). Additionally, the peak at 279.8 eV confirms the bond between carbon and metals (Ti–C/Ni–C).[35] The C 1s peak, originally at 284.8 eV, shifts towards a higher binding energy of 286.6 eV, indicating surface oxidation.[36] In the Ni 2p region spectra of $MOF@Ti_3C_2T_x$(Ti–N), peaks at 853.5 eV and 870.8 eV are assigned to Ni $2p_{3/2}$ and Ni $2p_{1/2}$, respectively (Fig. 2(e)), confirming the metallic behavior of Ni. The N 1s spectrum of $MOF@Ti_3C_2T_x$ (Ti–N) shifts towards lower binding energy compared to the N 1s peak of pristine $Ni_3(HITP)_2$-MOF, indicating

a higher concentration of C=N–C bonds relative to C–NH–C bonds. This shift suggests a favorable environment for nitrogen–metal bonding, further supporting the strong interaction between the MOF and MXene (Fig. 2(f)).[37] Further deconvolution of the N 1s spectrum reveals two distinct peaks at 395.1 eV and 397.3 eV, corresponding to titanium–nitrogen (Ti–N) and carbon–nitrogen (C=N) bonds, respectively (Fig. 2(f)). Additionally, the disappearance of the C–N–O peak after annealing indicates that the termination groups (O, OH) in the MXene are replaced by nitrogen, further supporting the formation of Ti–N bonding.[38]

By controlling the composition of the MOF on $Ti_3C_2T_x$-MXene through *in situ* synthesis, we optimized $MOF@Ti_3C_2T_x$ for efficient HER activity. The electrocatalytic activity of $MOF@Ti_3C_2T_x$ was characterized in an alkaline (1.0 M KOH) electrolyte. We first compared the HER activity of $MOF@Ti_3C_2T_x$ with different as-grown compositions of MOF on $Ti_3C_2T_x$-MXene using linear sweep voltammetry (LSV) curves at a scan rate of 10 mV s^{-1}, as shown in ESI Fig. S5(a).† In this study, all reported potentials were converted to the reversible hydrogen electrode (RHE) scale. The LSV curves indicate that $MOF@Ti_3C_2T_x$(33%HATP) has the lowest HER overpotential (207 mV) to achieve a current density of 10 mA cm^{-2} among the synthesized compositions of MOF and $Ti_3C_2T_x$-MXene: $MOF@Ti_3C_2T_x$(66%HATP) (331 mV), $MOF@Ti_3C_2T_x$(50%HATP)

(261 mV), and MOF@Ti$_3$C$_2$T$_x$(25%HATP) (330 mV). This confirms that fully continuous coverage of MOF on MXene is important to overcome the inherent limitations of MOFs, such as poor conductivity and limited stability, in achieving efficient HER activity. Furthermore, to investigate the effect of the chemical bond (Ti–N), LSV curves of the chemically bonded optimized composition of MOF@Ti$_3$C$_2$T$_x$ (MOF@Ti$_3$C$_2$T$_x$(Ti–N)) were obtained, as shown in Fig. 3(a). The LSV results of MOF@Ti$_3$C$_2$T$_x$(Ti–N) demonstrate enhanced electrocatalytic activity for the HER with a lower overpotential of 180 mV than the optimized as-grown MOF@Ti$_3$C$_2$T$_x$(33%HATP) (207 mV). This is three times lower than that of pristine Ni$_3$(HITP)$_2$-MOF (706 mV), and pristine Ti$_3$C$_2$T$_x$-MXene (670 mV). The result explicitly indicates that the chemical bond between the metal of Ti$_3$C$_2$T$_x$-MXene and the anion of Ni$_3$(HITP)$_2$-MOF plays a significant role in promoting the HER activity of MOF@Ti$_3$C$_2$T$_x$. In addition, compared to similar studies on MOF or MOF-derived electrocatalysts, particularly single-metallic 2D MOFs, the electroactivity of Ni$_3$(HITP)$_2$@Ti$_3$C$_2$T$_x$(Ti–N) demonstrates significant superiority in this field,[39–44] summarized in ESI Table S1.†

To analyze the reaction kinetics occurring on MOF@Ti$_3$C$_2$T$_x$, Tafel plots were obtained by the Tafel equation according to their LSV curves, as shown in Fig. 3(b). The Tafel slope of MOF@Ti$_3$C$_2$T$_x$(Ti–N) reaches 123 mV dec^{-1}, significantly lower than that of pristine Ni$_3$(HITP)$_2$-MOF (175 mV dec^{-1}) and pristine Ti$_3$C$_2$T$_x$-MXene (172 mV dec^{-1}). Moreover, the Tafel slope values of as-grown MOF on Ti$_3$C$_2$T$_x$-MXene MOF@Ti$_3$C$_2$T$_x$(66%

HATP), MOF@Ti$_3$C$_2$T$_x$(50%HATP), MOF@Ti$_3$C$_2$T$_x$(33%HATP) and MOF@Ti$_3$C$_2$T$_x$(25%HATP) are 240, 175, 165, and 204 mV dec^{-1}, respectively, as shown in ESI Fig. S5(b).† Among these samples, MOF@Ti$_3$C$_2$T$_x$(Ti–N) exhibits the smallest Tafel slope, indicating the fastest kinetics for HER electrocatalysis, thereby confirming the importance of the Ti–N bonds. For deeper insights into how the chemical bonding between MOF and MXene affects the reaction kinetics, we quantified the overall turnover frequencies (TOFs) per surface site, shown in Fig. 3(c) (detailed calculations are provided in the ESI†). The TOF value of MOF@Ti$_3$C$_2$T$_x$(Ti–N) is 0.59 s^{-1} at an overpotential of 200 mV, which is 10 times higher than that of pristine Ti$_3$C$_2$T$_x$-MXene (0.06 s^{-1}) and 30 times higher than that of pristine Ni$_3$(HITP)$_2$-MOF (0.02 s^{-1}). The TOF value of the optimized as-grown MOF on Ti$_3$C$_2$T$_x$-MXene, MOF@Ti$_3$C$_2$T$_x$(33%HATP), is 0.33 s^{-1}, which is 2 times lower than MOF@Ti$_3$C$_2$T$_x$(Ti–N). The higher TOF strongly correlates with the enhanced catalytic performance for the HER, indicating that the improved activity of MOF@Ti$_3$C$_2$T$_x$ is directly due to the chemical bonding between the MXene metal and MOF anions (Ti–N), which provides efficient active sites for electrocatalytic activity. Additionally, electrochemical impedance spectroscopy (EIS) was utilized to determine the charge-transfer resistance (R_{ct}), as shown in Fig. 3(d). The R_{ct} of chemically bonded MOF@Ti$_3$C$_2$T$_x$(Ti–N) is 3 times lower (30.0 Ω) than that of pristine Ni$_3$(HITP)$_2$-MOF (93.0 Ω) and 2.5 times lower than that of pristine Ti$_3$C$_2$T$_x$-MXene (71.0 Ω). Additionally, R_{ct} of the as-grown MOF@Ti$_3$C$_2$T$_x$(33%HATP) exhibits a higher value (39.0 Ω s^{-1})
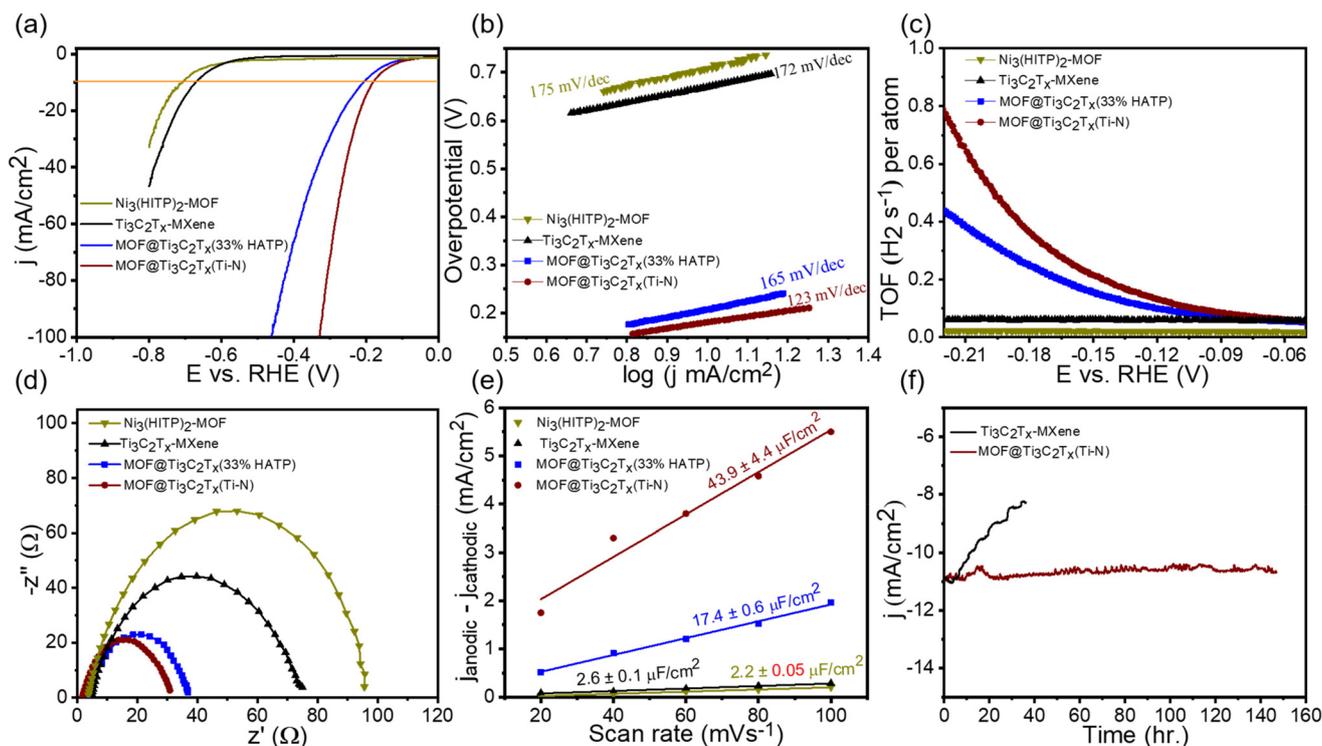
Fig. 3 Electrocatalytic performance for the HER of chemically bonded Ni$_3$(HITP)$_2$@Ti$_3$C$_2$T$_x$ in 1.0 M KOH. (a) Linear sweep voltammetry. (b) Tafel plots. (c) Calculated turnover frequencies (TOFs) for H$_2$ per active site. (d) Nyquist plots, derived from electrochemical impedance spectroscopy. (e) ECSA plots obtained by the extraction of the double-layer capacitance (C_{dl}). (f) Long-term stability (chronoamperometry) measurements.

than that of MOF@Ti$_3$C$_2$T$_x$(Ti–N). This aligns with the other kinetic measurements and suggests that the formation of the Ti–N chemical bonds facilitates charge transfer and provides more active sites for electrocatalytic activity.

To clarify the impact of the chemical bonding and continuous growth of MOF@Ti$_3$C$_2$T$_x$, we measured the electrochemically active surface area (ECSA) of the synthesized samples. This was done through cyclic voltammetry (CV) measurements to determine the electrical double-layer capacitance (EDLC) (C_{dl}), which is directly proportional to ECSA, as shown in ESI Fig. S6.† At each scan rate, the chemically bonded MOF@Ti$_3$C$_2$T$_x$(Ti–N) exhibits robust anodic and cathodic current densities with a quasi-rectangular shape, indicating a larger active surface area compared to the as-synthesized MOF@Ti$_3$C$_2$T$_x$(33%HATP). The plots showing differences in the variation of current density $vs.$ scan rate (Fig. 3(e)) reveal C_{dl} values of 43.9 μF cm^{-2} and 17.4 μF cm^{-2} for MOF@Ti$_3$C$_2$T$_x$(Ti–N) and MOF@Ti$_3$C$_2$T$_x$(33%HATP), respectively. The MOF@Ti$_3$C$_2$T$_x$(Ti–N) shows a 2.5 times higher C_{dl}, attributed to the chemical bonding between Ti and N, which exposes previously inaccessible metal active sites for efficient electrocatalytic activity. In addition to its high activity, MOF@Ti$_3$C$_2$T$_x$(Ti–N) demonstrates excellent electrochemical durability, maintaining stable performance at 200 mV with no significant decrease in activity after 150 hours of continuous HER, as shown in Fig. 3(f). This level of durability meets the set goals for DOE electrocatalysts.[45] In comparison, the stability of pristine Ti$_3$C$_2$T$_x$ MXene is inferior, confirming that the continuous growth of Ni$_3$(HITP)$_2$ MOF on the MXene enhances its durability in alkaline media. These results further validate that the stability of Ni$_3$(HITP)$_2$ MOF is superior to that of bimetallic MOFs, likely due to its strong chemical bonding with MXene and the absence of secondary metal-induced degradation pathways.[46] To evaluate the chemical and structural durability of MOF@Ti$_3$C$_2$T$_x$(Ti–N) in alkaline media, we conducted XPS and SEM analyses following electrochemical stability tests. The XPS results, shown in ESI Fig. S7,† indicate no significant changes in the chemical states of MOF@Ti$_3$C$_2$T$_x$(Ti–N). This suggests that the chemical bonding of the MOF on Ti$_3$C$_2$T$_x$ effectively prevents oxidation and corrosion of the transition metal surface, resolving stability issues in alkaline electrolytes. Additionally, SEM analysis (shown in ESI Fig. S8†) confirms structural stability, with no significant alterations observed.

To assess the general applicability of our chemically bonded MOF on Ti$_3$C$_2$T$_x$-MXene for electrolyzer integration, we conducted HER electrocatalytic activity tests in acidic media (0.5 M H$_2$SO$_4$). The chemically bonded MOF@Ti$_3$C$_2$T$_x$(Ti–N) exhibits outstanding performance, achieving a remarkably low overpotential of 240 mV at 10 mA cm^{-2}, which is 2.5 times lower than that of pristine Ti$_3$C$_2$T$_x$-MXene (750 mV) and two times lower than that of pristine Ni$_3$(HITP)$_2$-MOF (640 mV), as shown in Fig. 4(a). This result surpasses the overpotential of
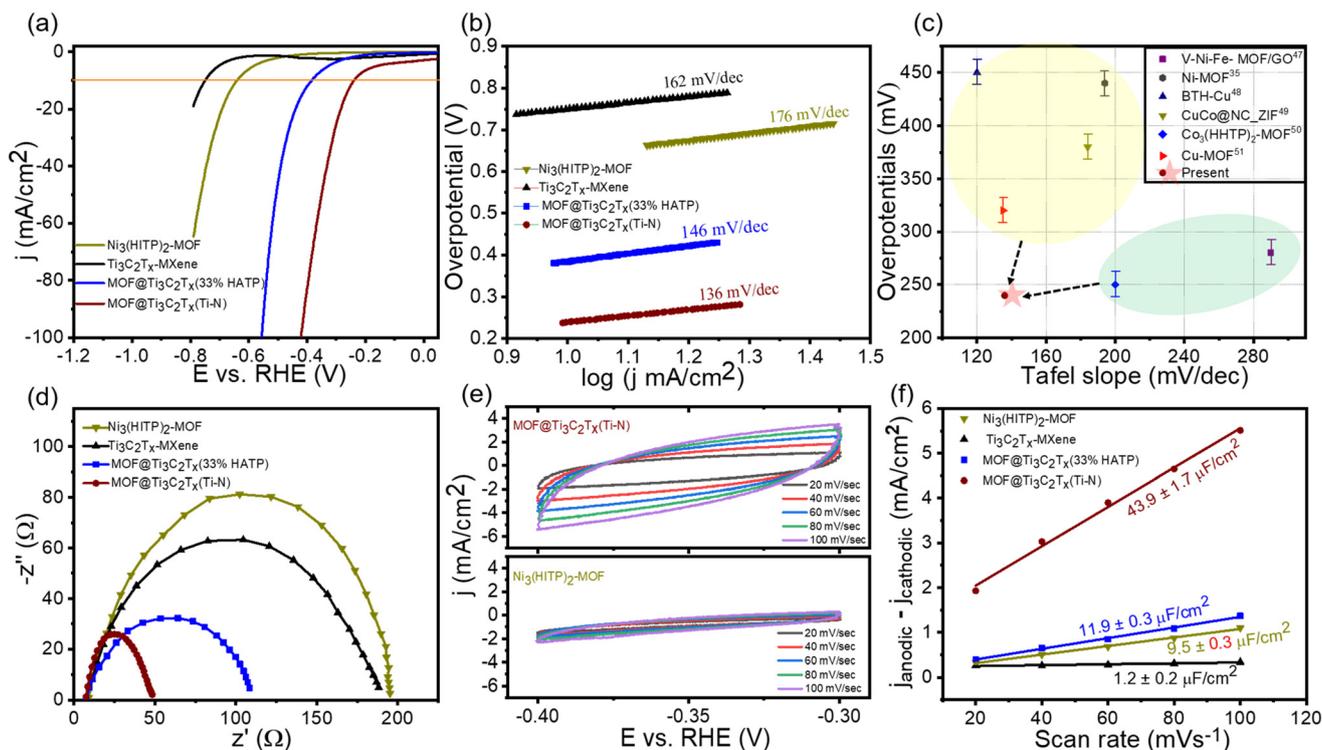
Fig. 4 Electrocatalytic performance for the HER of chemically bonded Ni$_3$(HITP)$_2$@Ti$_3$C$_2$T$_x$ in 0.5 M H$_2$SO$_4$. (a) Linear sweep voltammetry. (b) Tafel plots. (c) Comparison of overpotential at 10 mA cm^{-2} and Tafel slopes between Ni$_3$(HITP)$_2$@Ti$_3$C$_2$T$_x$ and other MOF-based electrocatalysts. (d) Nyquist plots, derived from electrochemical impedance spectroscopy. (e) Cyclic voltammetry of Ni$_3$(HITP)$_2$@Ti$_3$C$_2$T$_x$ and pristine Ni$_3$(HITP)$_2$-MOF. (f) ECSA plots obtained by the extraction of the double-layer capacitance (C_{dl}) from different 3D electrodes.

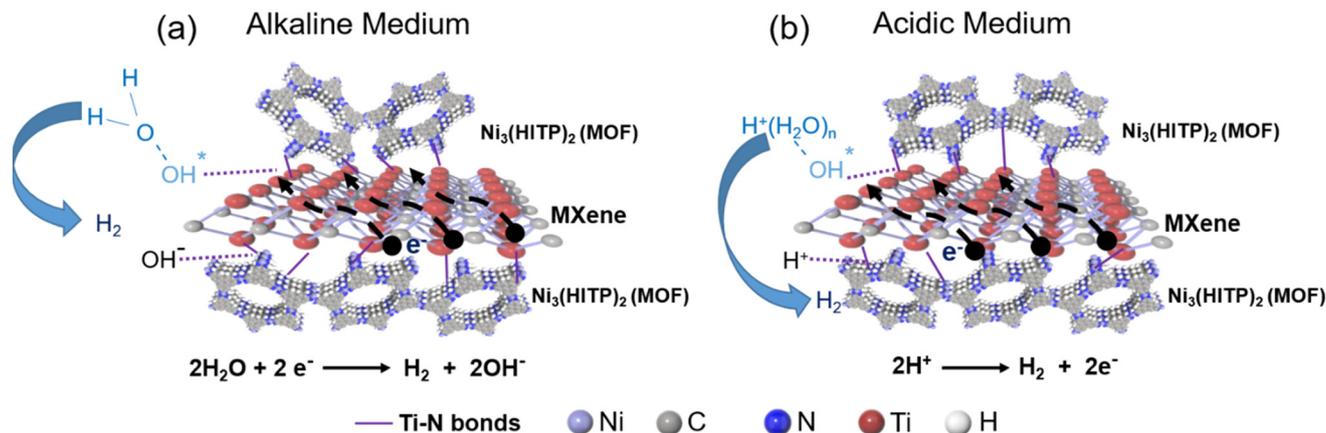**Fig. 5** Schematic illustration of the role of Ti–N bonds in promoting the HER on MOF@Ti$_3$C$_2$T$_x$ through the formation of strong non-covalent hydrogen bonding with the reactants (hydronium ions or water). (a) Proposed HER mechanism in an alkaline medium. (b) Proposed HER mechanism in an acidic medium.

leading PGM-free MOF-based electrocatalysts.[35,47–51] In contrast, the as-grown MOF@Ti$_3$C$_2$T$_x$(33%HATP) exhibits lower electrocatalytic activity with a higher overpotential (370 mV) compared to MOF@Ti$_3$C$_2$T$_x$(Ti–N). This result indicates that the Ti–N chemical bond provides more active sites for electrocatalytic activity. This finding suggests that efficient electrocatalytic performance for HER can be achieved by growing a chemically bonded MOF on a Ti$_3$C$_2$T$_x$-MXene to increase the number of active sites.

To understand the enhanced kinetics in acidic media, we extracted the Tafel plots from the polarization curves, as shown in Fig. 4(b). The Tafel slope of MOF@Ti$_3$C$_2$T$_x$(Ti–N) is approximately 136 mV dec^{-1}, which is the best among reported noble metal-free MOF-based electrocatalysts.[47,50] The comparison of electrocatalytic activity of MOF@Ti$_3$C$_2$T$_x$(Ti–N) with other reported noble metal-free MOF-based electrocatalysts is summarized in Fig. 4(c). Furthermore, we measured the charge transfer resistance (R_{ct}) of MOF@Ti$_3$C$_2$T$_x$(Ti–N), as shown in Fig. 4(d). The lower R_{ct} of MOF@Ti$_3$C$_2$T$_x$(Ti–N) (40 Ω), the smallest among the as-synthesized samples, further confirms that the chemical bond between the Ti of MXene and the N of MOF facilitates charge transfer in acidic media as well. Additionally, to confirm the enhancement in active sites, we calculated the ECSA from CV measurements. Similar to being under alkaline conditions, the chemically bonded MOF@Ti$_3$C$_2$T$_x$(Ti–N) shows higher anodic and cathodic current densities, indicating a significantly larger active surface area compared to pristine Ni$_3$(HITP)$_2$-MOF, as illustrated in Fig. 4(e) (CV of pristine Ti$_3$C$_2$T$_x$ and MOF@Ti$_3$C$_2$T$_x$(33%HATP) are shown in ESI Fig. S9†). The plots of variable current density *versus* scan rate (Fig. 4(f)) show that MOF@Ti$_3$C$_2$T$_x$(Ti–N) has a C_{dl} value of 43.9 μF cm^{-2}, which is four times greater than that of pristine Ni$_3$(HITP)$_2$-MOF (9.5 μF cm^{-2}). This indicates that MOF@Ti$_3$C$_2$T$_x$(Ti–N) provides more accessible active sites, leading to improved electrocatalytic activity in acidic media.

Up to this point, we have demonstrated that the chemically bonded MOF@Ti$_3$C$_2$T$_x$(Ti–N) significantly enhances HER activity in both acidic and alkaline media. To gain a fundamental understanding of this electrocatalyst's performance, we refer to our recent work which showed through density functional theory (DFT) studies that nitrogen-doped Ti$_3$C$_2$T$_x$-MXene with Ti–N bonds exhibits a lower Gibbs free energy for hydrogen adsorption ($\Delta G_H = -0.17$ eV) compared to pristine Ti$_3$C$_2$T$_x$-MXene ($\Delta G_H = -0.21$ eV),[24] providing optimal chemical adsorption behavior for electrocatalytic activity. Therefore, we focus on the effect of the chemical bonding between Ti and N in MOF@Ti$_3$C$_2$T$_x$(Ti–N) for electrocatalytic activity. Our hypothesis that the Ti–N bond promotes HER on MOF@Ti$_3$C$_2$T$_x$(Ti–N) electrodes is illustrated in Fig. 5. In this context, we consider Ti and Ni as active sites for the adsorption of H$^+$ and OH$^-$ ions, which are critical for the electrocatalytic activity. In alkaline media, we consider the mechanisms for overcoming kinetic barriers to water dissociation. At the Ti–N sites, while –OH attracts water to the surface, we propose that the splitting of water occurs at the metal (Ni) sites of the MOF, as shown in Fig. 5(a). The moderate adsorption energy for OH on Ti–N leads to an easy HO–H bond cleavage with the formation of adsorbed H*, followed by the removal of the second –OH site, restoring the structure to its original state.[52] In acidic media, protons migrate to the energetically preferred metal sites (Ni) of the MOF and are reduced by one electron to produce Ti–N*–H. Finally, another proton from an adjacent H$^+$(H$_2$O)$_n$ reacts with the first H$^+$ to generate H$_2$, as shown in Fig. 5(b).

Conclusions

In summary, we have developed a hybrid electrocatalyst composed of Ni$_3$(HITP)$_2$-MOF chemically bonded to Ti$_3$C$_2$T$_x$-MXene (MOF@Ti$_3$C$_2$T$_x$(Ti–N)). The *in situ* synthetic method of

growing MOF on MXene allows for precise regulation of the chemical structure and composition of the resulting electrocatalyst. Benefiting from the chemical bond between the anion of the MOF and the metal from MXene, which improves intrinsic activity, the robustly integrated layered structures facilitate active site exposure, and the resulting MOF@$Ti_3C_2T_x$(Ti–N) electrocatalysts deliver excellent HER performance in both alkaline and acidic media. The optimized electrocatalyst achieves an overpotential of 180 mV at 10 mA cm^{-2} and a Tafel slope of 123 mV dec^{-1} in alkaline media, and an overpotential of 240 mV at 10 mA cm^{-2} and a Tafel slope of 136 mV dec^{-1} in acidic media, with outstanding durability of up to 150 hours. This work provides inspiration for designing noble metal-free MOF-based electrocatalysts and confirms our design concept of new conductive MOF materials for various energy conversion and storage applications.

Author contributions

APT and PC conceived the idea and conceptualized the project. MSR helped to perform the experiments. APT, PC, KAM, and WJS wrote the paper.

Data availability

The data that support the findings of this study are available from the corresponding author (WJS) upon reasonable request.

Conflicts of interest

There are no conflicts to declare.

Acknowledgements

References

1 Z. Cui, W. Jiao, Z. Huang, G. Chen, B. Zhang, Y. Han and W. Huang, *Small*, 2023, **19**, 2301465.

2 X. X. Wang, M. T. Swihart and G. Wu, *Nat. Catal.*, 2019, **2**, 578–589.

3 A. P. Tiwari, K. Kim and S. Jeon, *Curr. Opin. Electrochem.*, 2022, **34**, 100982.

4 A. P. Tiwari, T. G. Novak, X. Bu, J. C. Ho and S. Jeon, *Catalysts*, 2018, **8**, 551.

5 A. P. Tiwari, K. Lee, K. Kim, J. Kim, T. G. Novak and S. Jeon, *ACS Sustainable Chem. Eng.*, 2020, **8**, 17116–17123.

6 A. P. Tiwari, G. Bae, Y. Yoon, K. Kim, J. Kim, Y.-L. Lee, K.-S. An and S. Jeon, *ACS Sustainable Chem. Eng.*, 2023, **11**, 5229–5237.

7 K. Kim, A. P. Tiwari, G. Hyun, Y. Yoon, H. Kim, J. Y. Park, K.-S. An and S. Jeon, *J. Mater. Chem. A*, 2021, **9**, 7767–7773.

8 A. P. Tiwari, M. S. Rahman and W. J. Scheideler, *Adv. Mater. Technol.*, 2024, **13**, 2400160.

9 L. Kong, M. Liu, H. Huang, Y. Xu and X.-H. Bu, *Adv. Energy Mater.*, 2022, **12**, 2100172.

10 C.-P. Wang, Y.-X. Lin, L. Cui, J. Zhu and X.-H. Bu, *Small*, 2023, **19**, 2207342.

11 H.-F. Wang, L. Chen, H. Pang, S. Kaskel and Q. Xu, *Chem. Soc. Rev.*, 2020, **49**, 1414–1448.

12 W. Cheng, X. F. Lu, D. Luan and X. W. Lou, *Angew. Chem., Int. Ed.*, 2020, **59**, 18234–18239.

13 Y. Zhao, X. F. Lu, Z.-P. Wu, Z. Pei, D. Luan and X. W. Lou, *Adv. Mater.*, 2023, **35**, 2207888.

14 E. M. Miner, T. Fukushima, D. Sheberla, L. Sun, Y. Surendranath and M. Dincă, *Nat. Commun.*, 2016, **7**, 10942.

15 H. Zhang, H. Guo, J. Ren, X. Jin, X. Li and R. Song, *Chem. Eng. J.*, 2021, **426**, 131300.

16 Y. Zhou, L. Sheng, Q. Luo, W. Zhang and J. Yang, *J. Phys. Chem. Lett.*, 2021, **12**, 11652–11658.

17 S. B. Alahakoon, K. Tan, H. Pandey, S. D. Diwakara, G. T. McCandless, D. I. Grinffiel, A. Durand-Silva, T. Thonhauser and R. A. Smaldone, *J. Am. Chem. Soc.*, 2020, **142**, 12987–12994.

18 H. Huang, Y. Zhao, Y. Bai, F. Li, Y. Zhang and Y. Chen, *Adv. Sci.*, 2020, **7**, 2000012.

19 H. Jia, Y. Yao, J. Zhao, Y. Gao, Z. Luo and P. Du, *J. Mater. Chem. A*, 2018, **6**, 1188–1195.

20 M. Bat-Erdene, M. Batmunkh, B. Sainbileg, M. Hayashi, A. S. R. Bati, J. Qin, H. Zhao, Y. L. Zhong and J. G. Shapter, *Small*, 2021, **17**, 2102218.

21 V. Ramalingam, P. Varadhan, H.-C. Fu, H. Kim, D. Zhang, S. Chen, L. Song, D. Ma, Y. Wang, H. N. Alshareef and J.-H. He, *Adv. Mater.*, 2019, **31**, 1903841.

22 Y. Yoon, A. P. Tiwari, M. Choi, T. G. Novak, W. Song, H. Chang, T. Zyung, S. S. Lee, S. Jeon and K.-S. An, *Adv. Funct. Mater.*, 2019, **29**, 1903443.

23 Y. Yoon, A. P. Tiwari, M. Lee, M. Choi, W. Song, J. Im, T. Zyung, H.-K. Jung, S. S. Lee, S. Jeon and K.-S. An, *J. Mater. Chem. A*, 2018, **6**, 20869–20877.

24 A. P. Tiwari, S. McBride, A. B. Hamlin, M. S. Rahman, J. E. Huddy, G. Hautier and W. J. Scheideler, *ACS Sustainable Chem. Eng.*, 2023, **11**, 12084–12092.

25 F. Yang, D. Hegh, D. Song, J. Zhang, K. A. S. Usman, C. Liu, Z. Wang, W. Ma, W. Yang, S. Qin and J. M. Razal, *Mater. Rep.: Energy*, 2022, **2**, 100079.

26 Y. Hou, M. Qiu, M. G. Kim, P. Liu, G. Nam, T. Zhang, X. Zhuang, B. Yang, J. Cho, M. Chen, C. Yuan, L. Lei and X. Feng, *Nat. Commun.*, 2019, **10**, 1392.

27 T. Liu, P. Li, N. Yao, G. Cheng, S. Chen, W. Luo and Y. Yin, *Angew. Chem., Int. Ed.*, 2019, **58**, 4679–4684.

28 A. Dolbecq, E. Dumas, C. R. Mayer and P. Mialane, *Chem. Rev.*, 2010, **110**, 6009–6048.

29 R. M. Stolz, A. Mahdavi-Shakib, B. G. Frederick and K. A. Mirica, *Chem. Mater.*, 2020, **32**, 7639–7652.

30 D. Sheberla, L. Sun, M. A. Blood-Forsythe, S. Er, C. R. Wade, C. K. Brozek, A. Aspuru-Guzik and M. Dincă, *J. Am. Chem. Soc.*, 2014, **136**, 8859–8862.

31 M. Ghidiu, S. Kota, V. Drozd and M. W. Barsoum, *Sci. Adv.*, 2018, **4**, eaao6850.

32 M. K. Smith and K. A. Mirica, *J. Am. Chem. Soc.*, 2017, **139**, 16759–16767.

33 Thermally Reduced Graphene/MXene Film for Enhanced Li–ion Storage - Xu - 2018 - Chemistry – A European Journal - Wiley Online Library, **https://chemistry-europe. onlinelibrary.wiley.com/doi/10.1002/chem.201805162? msockid=38076405298c6c1316796b0928c76de3**, (accessed March 4, 2025).

34 L. C. Agudelo, R. Ospina, H. A. Castillo and A. Devia, *Phys. Scr.*, 2008, **2008**, 014006.

35 L. Fan, P. F. Liu, X. Yan, L. Gu, Z. Z. Yang, H. G. Yang, S. Qiu and X. Yao, *Nat. Commun.*, 2016, **7**, 10667.

36 T. Zhang, Y. Wu, Y. Yin, H. Chen, C. Gao, Y. Xiao, X. Zhang, J. Wu, B. Zheng and S. Li, *Appl. Surf. Sci.*, 2022, **572**, 151479.

37 C. M. Goodwin, Z. E. Voras, X. Tong and T. P. Beebe, *Coatings*, 2020, **10**, 967.

38 P. M. Korusenko, S. N. Nesov, S. N. Povoroznyuk, P. V. Orlov, D. N. Korotaev, K. N. Poleschenko and E. E. Tarasov, *Data Brief*, 2019, **27**, 104737.

39 X. F. Lu, L. Yu, J. Zhang and X. W. (David) Lou, *Adv. Mater.*, 2019, **31**, 1900699.

40 W. Cheng, H. Zhang, D. Luan and X. W. (David) Lou, *Sci. Adv.*, 2021, **7**, eabg2580.

41 Q. Qiu, T. Wang, L. Jing, K. Huang and D. Qin, *Int. J. Hydrogen Energy*, 2020, **45**, 11077–11088.

42 M. Liu, W. Zheng, S. Ran, S. T. Boles and L. Y. S. Lee, *Adv. Mater. Interfaces*, 2018, **5**, 1800849.

43 H. Xu, B. Fei, G. Cai, Y. Ha, J. Liu, H. Jia, J. Zhang, M. Liu and R. Wu, *Adv. Energy Mater.*, 2020, **10**, 1902714.

44 J. Duan, S. Chen and C. Zhao, *Nat. Commun.*, 2017, **8**, 15341.

45 S. T. Thompson, A. R. Wilson, P. Zelenay, D. J. Myers, K. L. More, K. C. Neyerlin and D. Papageorgopoulos, *Solid State Ionics*, 2018, **319**, 68–76.

46 S. Li, Y. Gao, N. Li, L. Ge, X. Bu and P. Feng, *Energy Environ. Sci.*, 2021, **14**, 1897–1927.

47 S. Gopi, A. Panda, A. G. Ramu, J. Theerthagiri, H. Kim and K. Yun, *Int. J. Hydrogen Energy*, 2022, **47**, 42122–42135.

48 X. Huang, H. Yao, Y. Cui, W. Hao, J. Zhu, W. Xu and D. Zhu, *ACS Appl. Mater. Interfaces*, 2017, **9**, 40752–40759.

49 M. Kuang, Q. Wang, P. Han and G. Zheng, *Adv. Energy Mater.*, 2017, **7**, 1700193.

50 X. Wu, W. Xu, Z. Wang, H. Li, M. Wang, D. Zhang, J. Lai and L. Wang, *Chem. Eng. J.*, 2022, **431**, 133247.

51 M. Jahan, Z. Liu and K. P. Loh, *Adv. Funct. Mater.*, 2013, **23**, 5363–5372.

52 R. Subbaraman, D. Tripkovic, K.-C. Chang, D. Strmcnik, A. P. Paulikas, P. Hirunsit, M. Chan, J. Greeley, V. Stamenkovic and N. M. Markovic, *Nat. Mater.*, 2012, **11**, 550–557.